International Journal of Heat and Fluid Flow 71 (2018) 353–365

Contents lists available at ScienceDirect

International Journal of Heat and Fluid Flow

journal homepage: www.elsevier.com/locate/ijhff

Gas–liquid flow of sub-millimeter bubbles at low void fractions: Experimental study of bubble size distribution and void fraction

Sotiris P. Evgenidis, Thodoris D. Karapantsios*

Department of Chemical Technology and Industrial Chemistry, Faculty of Chemistry, Aristotle University, University Box 116, 541 24 Thessaloniki, Greece

ARTICLE INFO

Keywords:
Void fraction
Bubble size distribution
Bubbly flow
Image analysis
Electrical resistance tomography
Differential pressure

ABSTRACT

This work studies gas–liquid flow of small bubbles (<1 mm) at low void fractions ($<10^{-1}$) that is encountered in human bloodstream during Decompression Sickness and is also relevant to two-phase applications such as flow boiling in macro-channels. Two fundamental parameters are experimentally investigated: Bubble Size Distribution (*BSD*) and void fraction. Experiments are conducted in co-current upward bubbly flow. Water and blood simulant are used as test liquids, while bubble size is controlled using prescribed surfactant (*SDS*) concentrations. *BSD*s are determined employing digital image analysis of bubbly flow images captured at three radial positions across the flow cross-section. Volumetric and cross-sectional area averaged void fraction is measured at three axial locations along the flow by Differential Pressure (ΔP) and Electrical Resistance Tomography (*ERT*), respectively. *BSD*s are well-fitted by the log-normal distribution. *ERT* and ΔP measurements are in fair agreement, with void fraction being practically equal along the flow. The influence of gas/liquid phase velocities and surfactant concentration on the measured void fraction and *BSD*s' average value and width is discussed in detail. Interestingly, high *SDS* concentration in blood simulant results in the formation of bubble clusters, whose role on the examined parameters is investigated.

1. Introduction

Gas–liquid flow is the most common type of two-phase flow that covers numerous phenomena of both industrial and academic significance. Bubbly flows are specific cases of two-phase flows where the gas phase is dispersed in the form of numerous, discrete bubbles inside the continuous liquid phase. In common processes, bubbles vary widely in size and shape and are much smaller than the diameter of their container. Bubbly flow is observed frequently in diverse engineering systems covering petroleum processing, oil and gas extraction and transportation, boilers, steam generators in nuclear reactors, electronic cooling and various types of chemical reactors (Julia and Hibiki, 2011; Shen et al., 2017). Also, it can be encountered in the human bloodstream during either open heart surgery with extracorporeal circulation due to hardware malfunction (Mino et al., 2015) or during Decompression Sickness incidents, e.g. in scuba divers, metro workers and astronauts (Papadopoulou et al., 2015; Oikonomidou et al., 2018). The former case typically refers to a few bubbles of fixed size scaling from millimeters to micrometers that accidentally enter the blood circulation during surgery whereas the latter case refers to a cloud of growing bubbles of sub-millimeter size that form directly inside the blood by desorption of dissolved breathing nitrogen in the blood.

Void fraction (volumetric gas fraction) and Bubble Size Distribution (*BSD*) are fundamental two-phase flow parameters. They enable the computation of interfacial area, which is the main parameter for the evaluation of heat and mass transfer at the interface. Additionally, void fraction and *BSD* information are necessary to properly set-up a Computational Fluid Dynamics model. Consequently, the concept of void fraction and *BSD* have been attractive for researchers resulting in several measuring techniques (Besagni and Inzoli, 2016; Bhagwat and Ghajar, 2014).

BSD in a two-phase system can be measured by several methods divided mainly in two categories: intrusive and non-intrusive. Intrusive methods include capillary suction probes, conductivity probes, optical fiber probes and wire-mesh sensors. Non-intrusive methods employ interferometric particle imaging, laser Doppler velocimetry, phase Doppler anemometry and other particle image techniques. In general, non-intrusive techniques are preferred over the intrusive ones because they do not disturb flow conditions (Karn et al., 2015). A classical non-intrusive method is applied in this study, which is the photographic technique in association with digital image analysis. Due to its simplicity, flexibility and low cost, the classic photographic method is the preferred tool for precise bubble size measurement (Gaillard et al., 2015). However, implementation of this method faces several

* Corresponding author.
E-mail address: karapant@chem.auth.gr (T.D. Karapantsios).

https://doi.org/10.1016/j.ijheatfluidflow.2018.04.011
Received 30 November 2017; Received in revised form 20 April 2018; Accepted 20 April 2018
Available online 08 May 2018
0142-727X/

Nomenclature

α	void fraction
ΔP	Differential pressure
$\Delta P_{0,Usl}$	pressure difference when $U_{sg} = 0$ ($\alpha = 0$)
$\Delta P_{local,1}$	differential pressure sensor providing local measurement of void fraction for a flow length of 7.0 cm, at a distance $z/D = 10$ from the gas injection point
$\Delta P_{local,2}$	differential pressure sensor providing local measurement of void fraction for a flow length of 7.0 cm, at a distance $z/D = 55$ from the gas injection point
$\Delta P_{overall}$	differential pressure sensor providing overall void fraction measurement in the vertical tube for a flow length of 87.0 cm, at a distance $z/D = 33$ from the gas injection point
μ	scale parameter of log-normal distribution
μ_l	liquid dynamic viscosity
ρ_l	liquid density
σ	shape parameter of log-normal distribution
BSD	bubble size distribution
CV	coefficient of variation
C_{SDS}	concentration of SDS
D	internal pipe diameter
$D_{1,0}$	arithmetic mean bubble diameter
$D_{3,2}$	Surface weighted mean bubble diameter
$D_{4,3}$	Volume weighted mean bubble diameter
DCS	Decompression Sickness
ERT	Electrical Resistance Tomography
ERT1	ERT probe for void fraction measurement at a distance $z/D = 10$ from the gas injection point
ERT2	ERT probe for void fraction measurement at a distance $z/D = 30$ from the gas injection point
ERT3	ERT probe for void fraction measurement at a distance $z/D = 55$ from the gas injection point
$ERT_{average}$	average value from *ERT1, ERT2, ERT3* void fraction measurements
R	correlation coefficient
r	radial distance from the pipe center
SDS	Sodium Dodecyl Sulfate
U_{sg}	gas superficial velocity
U_{sl}	liquid superficial velocity
Re_l	liquid phase Reynolds number (defined by $\rho_l U_{sl} D/\mu_l$)
z/D	normalized axial distance

challenges. For instance, a large number of bubbles may be overlapping (~40%) even at low void fraction (~1%). In that case, many image-processing algorithms underestimate bubble size (Besagni and Inzoli, 2016). Various studies have addressed this problem and have proposed different methods for dealing with overlapping bubbles (Lau et al., 2013; Zabulis et al., 2007).

Non-invasive techniques for the measurement of void fraction include pressure drop, dynamic gas disengagement, conductimetry, light attenuation, neutron/γ-ray/X-ray absorption, ultrasound attenuation, NMR and γ- or X-ray/capacitive or resistive/ultrasonic tomography (Kanizawa and Ribatski, 2017; Uesawa et al., 2012). Among these techniques, two well-established methods for void fraction determination in two-phase systems are of interest to this study: Differential Pressure (*ΔP*) and Electrical Resistance Tomography (*ERT*) for volumetric and cross-sectional area averaged void fraction estimation, respectively, inside a vertical pipe. The use of these two methods allows the comparison of void fraction measurements at different sites along the flow and further increases the confidence to void fraction measurements.

Measuring void fraction via a pressure difference is simple. This technique does not require a transparent fluid or vessel and also does not have requirements on liquid electrical properties. It can be used to measure the overall average void fraction in a multiphase column, as well as the local average void fraction in a column section. Thus, it can be used to probe the axial void fraction variation in a column (Han et al., 2016; Tang and Heindel, 2006).

ERT is considered the most powerful tool among other available tomography techniques due to its high-speed capability, low construction cost, high safety and suitability for small or large vessels (Jin et al., 2013). It provides temporal–spatial information of multiphase flow at one or multiple measuring cross sections of a vessel. *ERT* is sensitive to the resistance change of a fluid and thus it is suitable for gas–liquid two-phase flow when the liquid phase is a conductive fluid. Several works have been carried out for concentration profile visualization and void fraction determination in gas–liquid two-phase systems employing *ERT* (Fransolet et al., 2005; Jin et al., 2010; Jin et al., 2006; Meng et al., 2010).

The objective of this study is to experimentally investigate void fraction and bubble size distribution in vertical co-current upward two-phase flow, where the examined conditions resemble bubbly flow in human vena cava during Decompression Sickness, *DCS* (Vann et al., 2011). Better understanding of bubbly flow characteristics is expected to facilitate CFD modeling of *DCS* and therefore to contribute in the prevention and treatment of the disease. Such bubbly flow conditions, combining sub-millimeter bubbles and low void fractions ($<10^{-1}$), are also encountered in other two-phase flow applications, e.g., flow boiling in macro-channels (Maurus et al., 2002; Yoo et al., 2016). The present work is a follow-up of Evgenidis and Karapantsios (2015) that: a) expands 70% the previous data set to more experimental conditions, b) applies two commercial techniques, Electrical Resistance Tomography and Differential Pressure, instead of a custom-made electrical impedance technique for cross-sectional area averaged and volumetric void fraction determination, respectively, c) investigates void fraction evolution along the vertical pipe and d) provides comparative bubble size distributions to enhance the study of liquid properties and phase velocities on bubble size features. The next section presents the employed experimental techniques and materials. A section follows with experimental results on bubble size distribution and void fraction where descriptive statistics are used to describe and compare the data. Finally, a discussion is made regarding the influence of liquid phase physical properties and phase velocities on void fraction and bubble size.

2. Materials and methods

Measurements are conducted in a vertical co-current upward bubbly flow provided by a fully controllable flow loop. The liquid phase is recirculated through the flow loop by means of a progressive cavity pump (MD 025-6L, Motovario S.p.A.). The main part of the loop consists of a vertical tube 1.6 m long with internal diameter $D = 21$ mm. This is the diameter of human vena cava where bubbles gather during a decompression incident (Vann et al., 2011). Moreover, $D = 21$ mm is within the range of macro-channel diameters studied in flow boiling applications. Gas phase is injected through a cylindrical glass microporous filter (ROBU®; diameter: 12 mm, nominal pore size: 1.0–1.6 μm) located at the center of the bottom of the vertical tube, where the two phases come in contact. The top filter wall is covered with glue to avoid large bubbles exiting and so the only bubbles allowed to enter the liquid flow are those generated and sheared-off at the side filter wall. Continuous formation of bubbles facilitates in-vitro study of developed bubbly flow in human vena cava where bubbles gather during *DCS*. More details about the flow loop operation are found in Evgenidis and Karapantsios (2015). Along the vertical tube, successive test sections of

electrical, optical, acoustical and pressure diagnostics are employed for void fraction, bubble size and bubble velocity measurements. In this work, acoustical measurements were not performed. The schematic diagram of experimental setup is shown in Fig. 1, whereas the entire experimental setup is depicted in **Supplementary Fig. 1.**

Experiments are performed at 37 °C, same as the body temperature, with two different test liquids. The first one is an aqueous solution of NaCl (purity > 99.5%, Merck KGaA), henceforth called ***Water***, having electrical conductivity as of tap water. The second one is an aqueous solution of glycerol (purity > 99.5%, Panreac) and *NaCl*, henceforth called ***Blood***, simulating human blood physical properties (electrical conductivity ~7 mS/cm, dynamic viscosity 4–5 mPa·s, pH ~7.5) (Dorsey, 1940; Woodcock, 1975). All measured physical properties of the test liquids at 37 °C are shown in Table 1. Helium gas (purity 99.9996%, Air Liquide) is chosen for bubbles production due to its low solubility in the test liquids.

Measurements are conducted for two bubble populations having different average bubble sizes, both below 1 mm. Preliminary tests showed that the use of glass microporous filters of varying pore sizes could not provide such bubble populations. On the other hand, the addition of 5 ppm and 500 ppm of the surface active agent sodium dodecyl sulphate (*SDS*, purity > 99.0%, Fluka Biochemika) in *Water* resulted in fairly distinct bubble size distributions. This is also the case for *Blood* between the absence and the presence of 500 ppm *SDS*. Further, this enables the investigation of surfactant concentration influence on void fraction and *BSD* features as well.

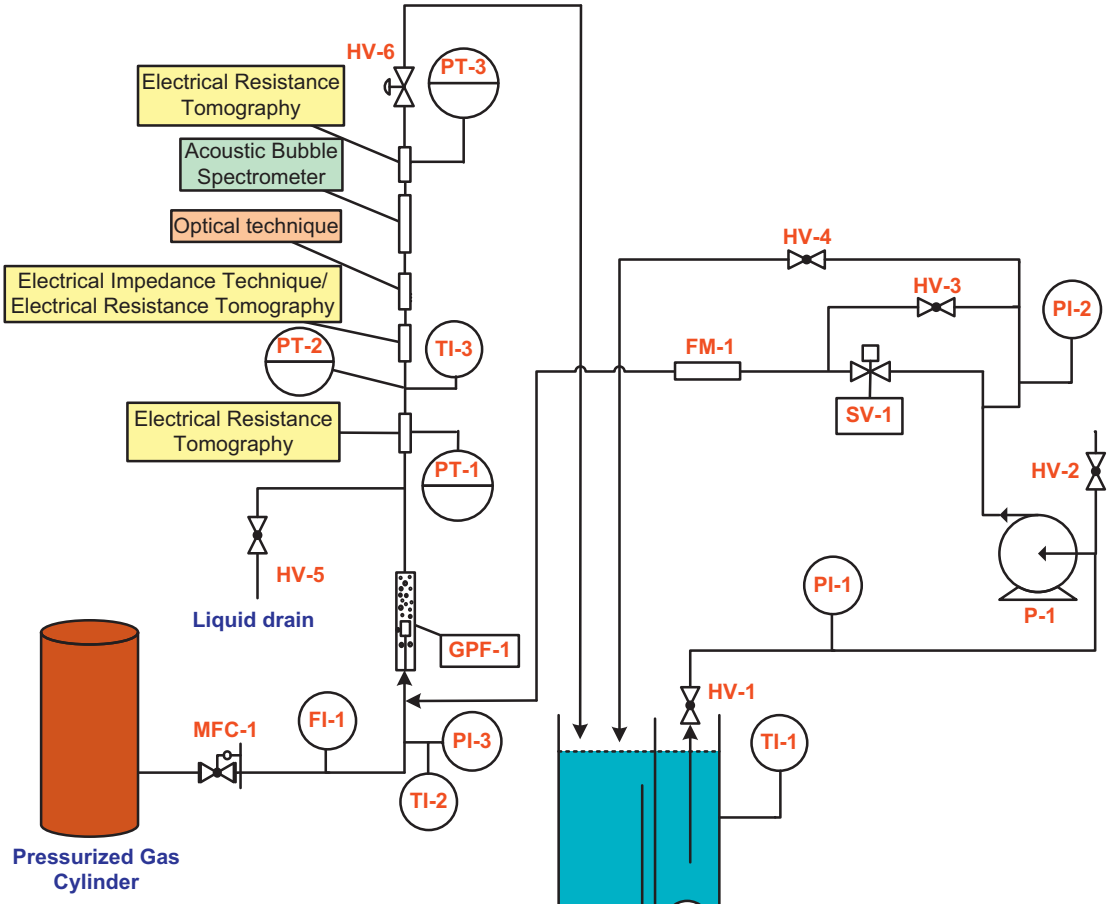

Code	Description
T-1	Liquid Tank
P-1	Progressive Cavity Pump
SV-1	Proportional Electromagnetic Valve
HC-1	Heater/Circulator
FM-1	Liquid Flow Meter
MFC-1	Gas Mass Flow Controller
FI-1	Gas Flow Meter
GPF-1	Glass Porous Filter
HV-1,2,3,4,5	On/Off Hand Valves
HV-6	Screw Down Hand Valve
TI-1,2,3	Temperature Indicators
PI-1,2,3	Pressure Indicators
PT-1,3	Differential Pressure Transducers
PT-2	Absolute Pressure Transducer

Fig. 1. Schematic diagram of experimental setup.

Table 1
Measured physical properties of the employed test liquids at 37 °C.

Test liquid	Composition	C_{SDS} (ppm)	Static Surface tension (mN/m)	Density (kg/m^3)	Electrical conductivity (mS/cm)	Dynamic viscosity (mPa·s)
Water	NaCl (0.02% w/w) aqueous solution	5	67.0	995	0.63	0.70
		500	37.0	991	0.63	0.70
Blood	Glycerol (56.0% w/w)/NaCl (1.3% w/w) aqueous solution	–	68.0	1149	6.85	4.85
		500	34.0	1144	6.85	5.10

Cross-sectional area averaged and volumetric void fraction measurements along the vertical tube are conducted synchronously applying, respectively: a) an Electrical Resistance Tomography (*ERT*) technique (P2000, ITS) and b) three ultra-sensitive differential pressure (ΔP) sensors (DP 15, Validyne) combined with a proper signal demodulator (CD280, Validyne) and a 16 bit data acquisition card (DAQPad-6015, National Instruments). Details about the employed *ERT* system and the image reconstruction procedure can be found in Lioumbas et al. (2014).

Three similar probes, each consisting of 16 flush-mounted plate electrodes (2 mm × 2 mm) made of stainless steel (Fig. 2a and **Supplementary Fig. 2a**), run the circumference of the tube at three different heights (planes) in the vertical tube providing simultaneous *ERT* measurements at the three probe planes. The axial distances of *ERT* probes from the gas injection point are 21.5 cm for *ERT1* (z/D = 10), 62.0 cm for *ERT2* (z/D = 30) and 116.5 cm for *ERT3* (z/D = 55). A sinusoidal current (excitation) signal with a frequency of 9600 Hz and amplitude of 1–2 mA for *Water* and 12–14 mA for *Blood* is injected sequentially across each *ERT* probe plane. Voltage measurements are acquired from all combinations of electrode pairs to deliver a cross-sectional image of the tube reconstructed at a sampling frequency of 16 Hz. Preliminary tests showed that *Sensitivity Conjugate Gradients* reconstruction algorithm provides the maximum resolution, while void fraction is determined from electrical resistance data employing Maxwell's model (Maxwell, 1892). Consequently, the resolution of void fraction measurement is 0.001. Moreover, calibration tests conducted in bubble column monitoring liquid level rise, showed that void fraction measurement accuracy employing *ERT* is 0.5%. In this study, *ERT* measurements focus on the determination of average void fraction across each plane. Nonetheless, bubbly flow symmetry across the pipe is confirmed for all experimental conditions (Chatzidafni et al., 2009). Representative ERT images are shown in Evgenidis and Karapantsios (2015).

Volumetric void fraction (α) is determined through ΔP measurements applying Eq. (1), where $\Delta P_{0,Usl}$ is the pressure difference when $U_{sg} = 0$ ($\alpha = 0$) and U_{sl} is the same superficial liquid velocity at which ΔP is measured (Tang and Heindel, 2006):

$$\alpha = 1 - \frac{\Delta P}{\Delta P_{0,U_{sl}}} \quad (1)$$

Eq. (1) accounts for the effect of wall shear stress but neglects the effect of liquid acceleration due to void changes which however is considered negligible for the conditions of this study (Hills, 1976; Merchuk and Stein, 1981; Tang and Heindel, 2007). ΔP measurements are recorded at a sampling frequency of 500 Hz. Two sensors ($\Delta P_{local,1}$, $\Delta P_{local,2}$) provide local measurements of void fraction for a flow length of 7.0 cm using custom-made test sections (Fig. 2b and **Supplementary Fig. 2b**). A third one ($\Delta P_{overall}$) determines the overall void fraction in the vertical tube for a flow length of 87.0 cm incorporating the locations of $\Delta P_{local,1}$, $\Delta P_{local,2}$. The resolution of void fraction measurement is equal to that of ERT method (0.001), while measurement accuracy was shown to be 0.5% based on calibration tests in bubble column. The axial distances of the middle of the ΔP test sections from the gas injection point are 21.5 cm (z/D = 10) for $\Delta P_{local,1}$, 116.5 cm (z/D = 55) for $\Delta P_{local,2}$ and 68.5 cm (z/D = 33) for $\Delta P_{overall}$. Apparently, $\Delta P_{local,1}$ and $\Delta P_{local,2}$ measurements can be compared directly with *ERT1* and *ERT3* measurements, respectively, while $\Delta P_{overall}$ can be compared with the average value of the three *ERT* measurements along the vertical tube ($ERT_{average}$).

ERT and ΔP measurements are taken simultaneously with bubble size measurements using an optical method presented in Fig. 3 (Evgenidis et al., 2010). *BSD* determination is based on image processing of bubbly flow images captured at three radial positions inside the vertical tube (r = 0, r = D/4 and r = D/2) at an axial distance of 75 cm (z/D = 36) above the gas injection point, while a wire 56 μm thick is mounted at the outer surface of the tube as a reference scale. Images are taken using CANON EOS 350D still digital camera with a spatial resolution of 2.3 μm/pixel. The camera is equipped with proper macro lens (CANON EF100mm, f/2.8 Macro USM) and extension rings (CANON, 13-21-31 mm) to achieve the necessary magnification. As a result, the recorded optical window is 8.5 mm × 5.6 mm. Applied aperture values range from 2.8 to 7.1 that provide depth of field values ranging from 0.1 mm to 1 mm, respectively. Such low depth of field values are necessary to prevent overlapping of the captured optical windows for the three distinct radial positions inside the vertical tube. The camera is placed on a X-Y-Z micro-metering translation table

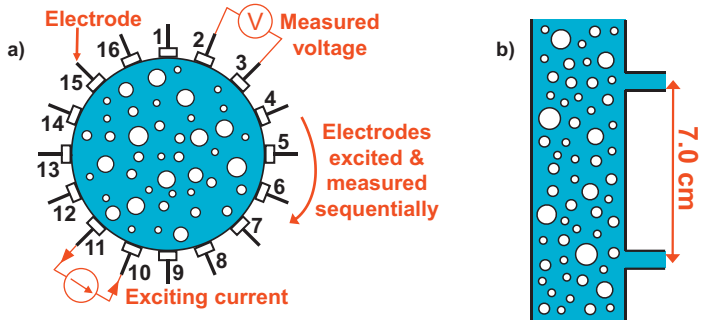

Fig. 2. Schematic drawings of: a) Electrical Resistance Tomography probe, b) Differential Pressure test section.

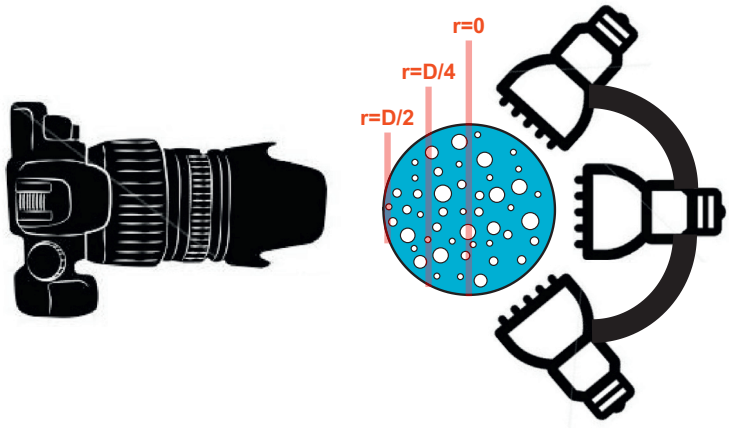

Fig. 3. Schematic representation of optical technique for *BSD* determination.

(Edmund Industrie Optik) to succeed focusing on a specific radial position inside the vertical pipe (**Supplementary Fig. 3a**). Additionally, a special multi-lighting system (**Supplementary Fig. 3b**) is used to provide adequate illumination even in dense bubbly flows. For each run, an average bubble size distribution is estimated by a custom-made software (**Supplementary Fig. 3c**) that exploits the template matching technique to discriminate and measure the size of overlapping, isolated bubbles (BubbleSEdit) (Zabulis et al., 2007). It analyzes series of images accumulating 500–1000 bubbles to achieve good statistical significance of estimations (Deckwer, 1992). Measurement accuracy is 4% as resulted from tests conducted using metallic spheres of certain size instead of bubbles. This software is applied to determine the size of isolated bubbles. However, bubble clusters are found to rise among numerous isolated bubbles under certain experimental conditions. In this case, the equivalent diameter of bubble clusters is estimated manually. Under the present experimental conditions, radial deviations were found negligible (Evgenidis et al., 2010), so the presented bubble sizes below are mean values over all the examined radial positions.

Five different liquid superficial velocities (2.89, 9.62, 16.36, 23.10, 29.83 cm/s) as well as eight different gas superficial velocities (0.048, 0.132, 0.217, 0.301, 0.385, 0.650, 0.914, 1.179 cm/s) are examined. Liquid superficial velocity values range from ~3 to ~30 cm/s, as these values are representative of bloodstream in human vena cava. On the other hand, gas superficial velocity values range from ~0.05 to ~1.2 cm/s providing average void fraction values between $\sim 10^{-3}$ and $\sim 10^{-1}$. It must be noted that this work is concerned only about average values of void fraction and not about void fraction fluctuations that in some of the present conditions momentarily goes down to even 10^{-5}, as experimentally noticed. In addition, it is noted that average void fraction values above $5*10^{-2}$ are high and not representative of usual *DCS* incidents in humans, yet they are important for the completeness of this study.

3. Results and discussion

3.1. Bubble size distribution study inside the vertical pipe

Typical bubble size distributions for the case of gas–liquid flow with small bubbles (<1 mm) at low void fractions ($<10^{-1}$) are given in Figs. 4–7. Figs. 4 and 5 concern *Water* for C_{SDS} = 5 ppm and C_{SDS} = 500 ppm, respectively, while Figs. 6 and 7 refer to *Blood* for C_{SDS} = 0 ppm and C_{SDS} = 500 ppm, respectively. Figs. 4–7 present totally 24 *BSDs* for the two extreme U_{sl} values (2.89 and 29.83 cm/s) and three U_{sg} values (0.048, 0.217 and 0.385 cm/s). 36 more *BSDs* for the intermediate U_{sl} values (9.62, 16.36 and 23.10 cm/s) and the three aforementioned U_{sg} values are shown in **Supplementary Figs. 4** and **5**,

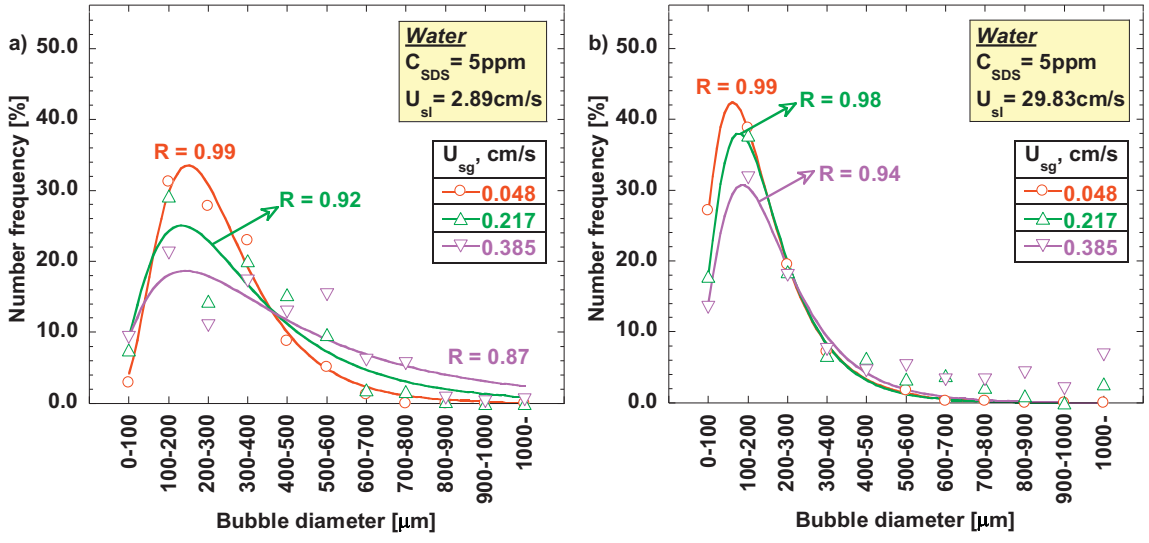

Fig. 4. Bubble Size Distributions for C_{SDS} = 5 ppm and U_{sg} = 0.048, 0.217, 0.385 cm/s in *Water*: a) U_{sl} = 2.89 cm/s, b) U_{sl} = 29.83 cm/s.

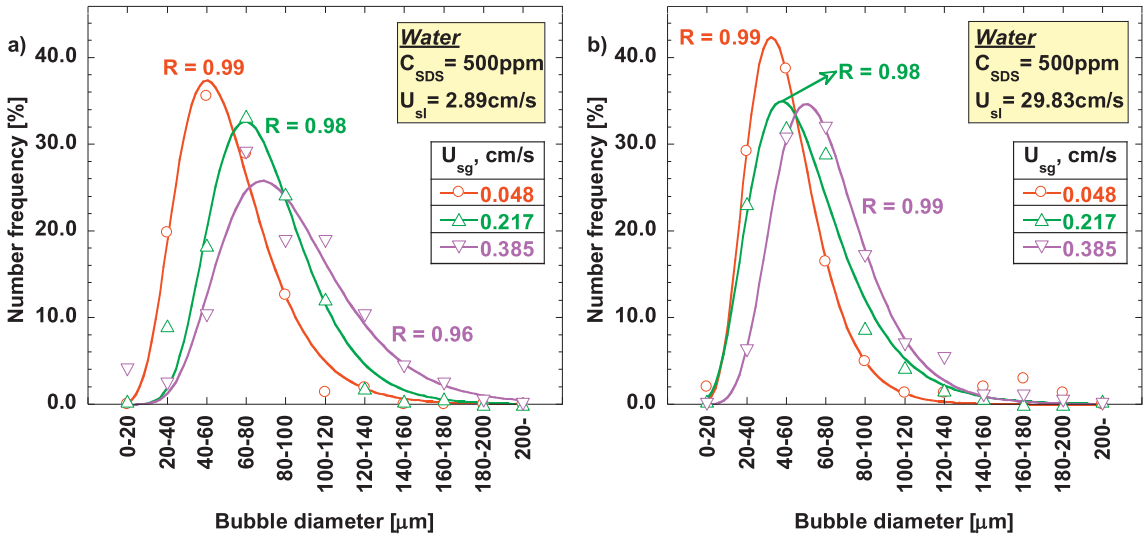

Fig. 5. Bubble Size Distributions for C_{SDS} = 500 ppm and U_{sg} = 0.048, 0.217, 0.385 cm/s in *Water*: a) U_{sl} = 2.89 cm/s, b) U_{sl} = 29.83 cm/s.

for *Water* and *Blood* respectively. Bins width has been properly chosen in each figure to represent the distribution correctly in the absence of abnormal spikes or smoothness. In all cases, *BSD* is not symmetrical (normal distribution) with an extended tail for the larger bubble sizes. This is characteristic of the log-normal distribution. Grau and Heiskanen (2005), Majumder et al. (2006) and Riquelme et al. (2015) have suggested that *BSD*s in such applications can be reasonably well-fitted with log–normal distributions. Consequently, this fitting is also applied to the present data. Goodness of fitting is denoted by the correlation coefficient *R* for each *BSD* in Figs. 4–7 and **Supplementary Figs. 4** and **5**. It is seen that most *BSD*s follow nicely the two-parameter log-normal distribution (*R*: 0.97 ± 0.02), whose equation is given below:

$$P(x) = \frac{1}{\sigma\sqrt{2\pi}x} e^{\frac{-(\ln(x)-\mu)^2}{2\sigma^2}} \quad (2)$$

Log-normal distributions are represented by two parameters: μ (scale parameter) that stretches or shrinks the distribution and σ (shape parameter) that affects the shape of the distribution (Antle, 1985). Parameters μ and σ designate the average and the standard deviation of the data after their logarithmic transformation. In this respect, Figs. 8 and 9 illustrate for all data sets (both test liquids and all experimental conditions) the average bubble diameter ($D_{1,0}$) and the coefficient of variation (*CV* = standard deviation/average), which are associated to μ and σ, respectively. This enables more efficient investigation of the role of U_{sg}, U_{sl} and C_{SDS} on *BSD* features (average diameter and width = variation around the average). Arithmetic mean bubble diameter ($D_{1,0}$) describes better the raw optical data as it is calculated directly from the recorded images. Besides, it is preferred over surface ($D_{3,2}$) or volume ($D_{4,3}$) weighted mean diameters due to the linearly spaced bubble size classes of *BSD*s (Merkus, 2009). However, an extended list of representative $D_{3,2}$ and $D_{4,3}$ values are given in **Supplementary Table 1** for convenience. The coefficient of variation is based on the normalization of the standard deviation with the average value and thus it is preferred over the standard deviation when the goal is the comparison of data with widely different average values.

Fig. 8a and b present $D_{1,0}$ as a function of U_{sl} for C_{SDS} = 5 ppm and C_{SDS} = 500 ppm in *Water,* respectively, for all U_{sg} values. Similarly, Fig. 9a and b display $D_{1,0}$ data for C_{SDS} = 0 ppm and C_{SDS} = 500 ppm in *Blood,* respectively. Fig 8c, d as well as Fig. 9c, d refer to coefficient of variation of $D_{1,0}$ for the same experimental conditions with Fig. 8a, b and Fig. 9a, b, respectively.

For the case of larger bubbles (C_{SDS} = 5 ppm in *Water* and

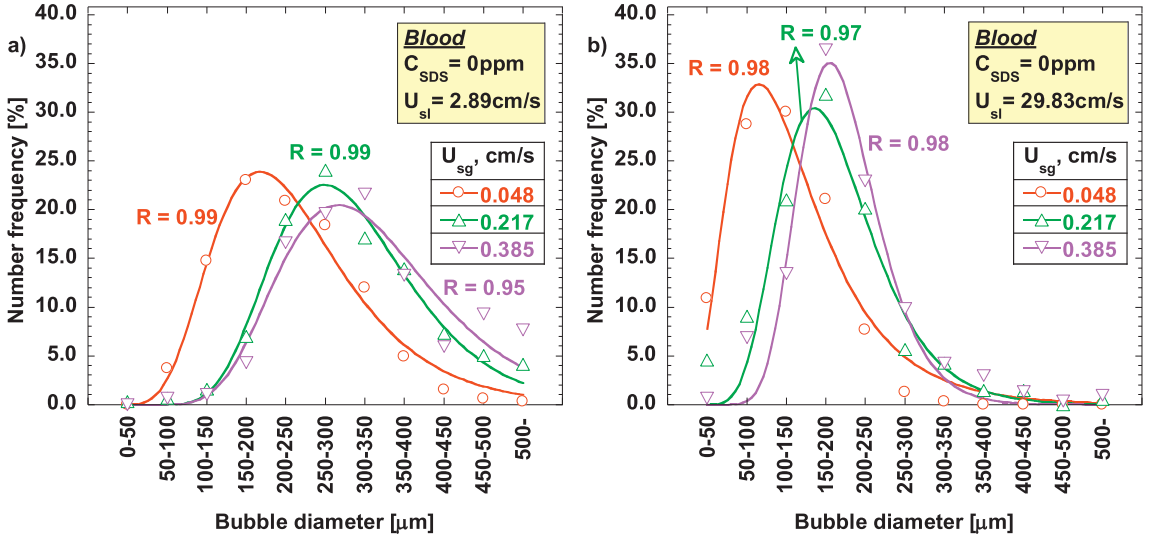

Fig. 6. Bubble Size Distributions for C_{SDS} = 0 ppm and U_{sg} = 0.048, 0.217, 0.385 cm/s in *Blood*: a) U_{sl} = 2.89 cm/s, b) U_{sl} = 29.83 cm/s.

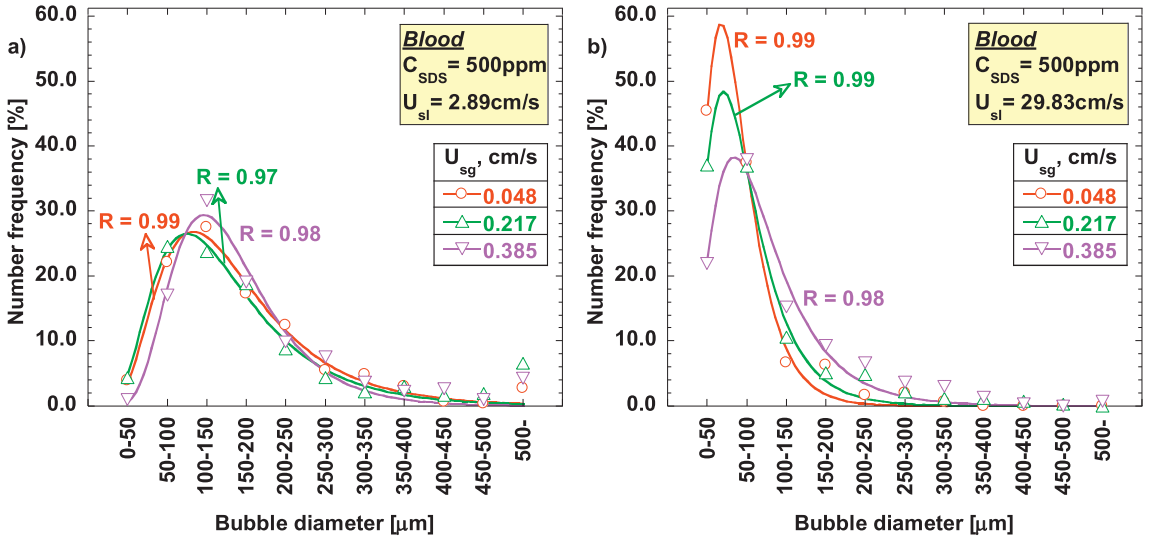

Fig. 7. Bubble Size Distributions for C_{SDS} = 500 ppm and U_{sg} = 0.048, 0.217, 0.385 cm/s in *Blood*: a) U_{sl} = 2.89 cm/s, b) U_{sl} = 29.83 cm/s.

C_{SDS} = 0 ppm in *Blood*) it is apparent that U_{sg} affects the average value of *BSDs* but not their *CV* which appears scattered with respect to U_{sg}. For a specific U_{sl} value, as U_{sg} increases larger bubbles but also more bubbles are encountered in the pipe (see also Section 3.2). These large bubbles are due to the increased gas flow rate which makes bubble grow more before they detach from the porous filter but also due to their high collision probability and, consequently, their coalescence. Other researchers have also noticed similar behavior, e.g.

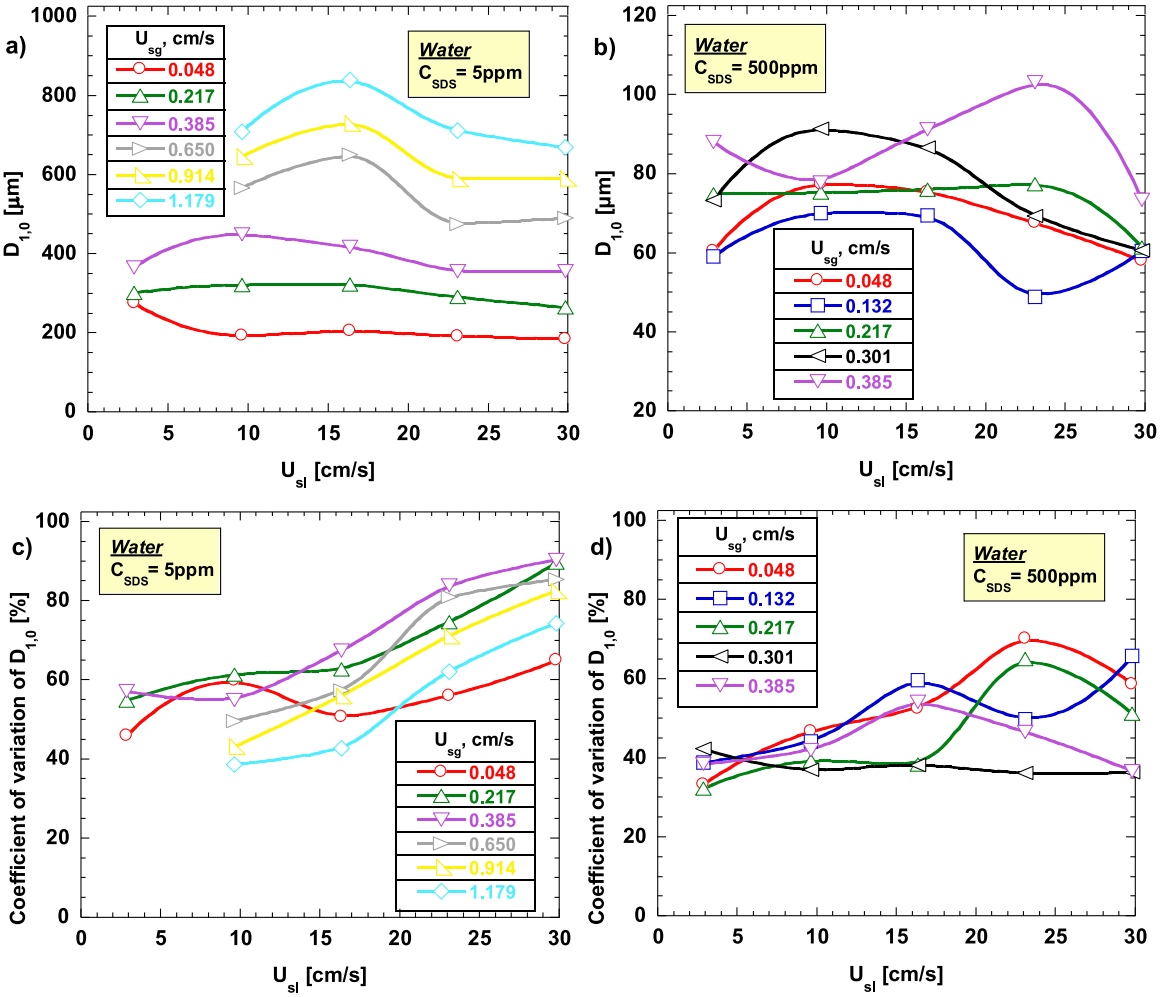

Fig. 8. Effect of superficial liquid velocity (U_{sl}) and superficial gas velocity (U_{sg}) on: a) arithmetic mean bubble diameter ($D_{1,0}$) for C_{SDS} = 5 ppm, b) arithmetic mean bubble diameter ($D_{1,0}$) for C_{SDS} = 500 ppm, c) coefficient of variation of $D_{1,0}$ for C_{SDS} = 5 ppm and d) coefficient of variation of $D_{1,0}$ for C_{SDS} = 500 ppm, in *Water*.

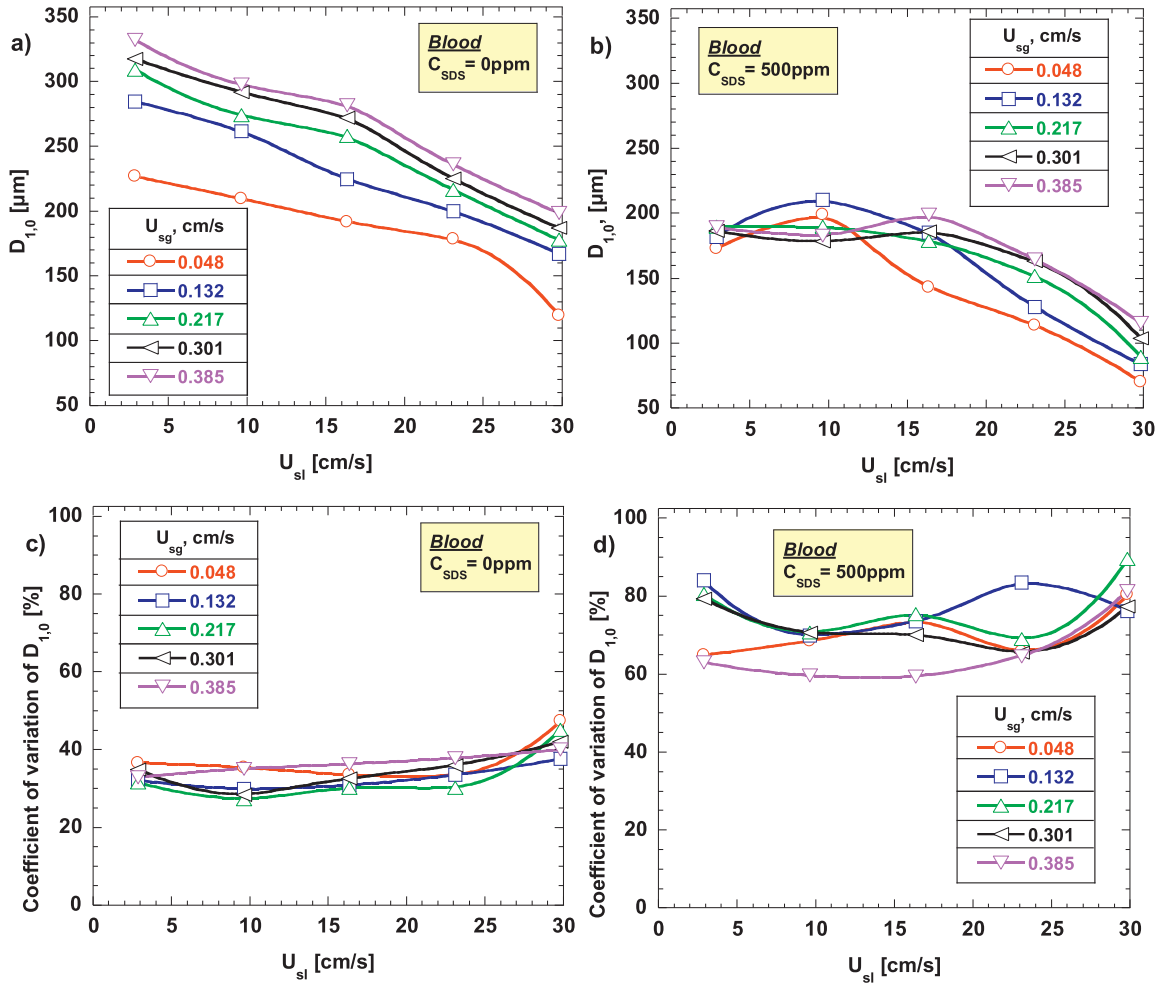

Fig. 9. Effect of superficial liquid velocity (U_{sl}) and superficial gas velocity (U_{sg}) on: a) arithmetic mean bubble diameter ($D_{1,0}$) for C_{SDS} = 0 ppm, b) arithmetic mean bubble diameter ($D_{1,0}$) for C_{SDS} = 500 ppm, c) coefficient of variation of $D_{1,0}$ for C_{SDS} = 0 ppm and d) coefficient of variation of $D_{1,0}$ for C_{SDS} = 500 ppm, in *Blood*.

Riquelme et al. (2015). Thus, *BSD* shifts to higher bubble sizes and so $D_{1,0}$ increases accordingly. On the contrary, for C_{SDS} = 500 ppm in *Water* and *Blood,* the influence of U_{sg} on average bubble size and width is less evident since the presence of surface active agent not only creates smaller bubbles by decreasing surface tension (Table 1) but also hinders bubbles coalescence by creating a viscoelastic film at the bubbles surface (Dutschk et al., 2014).

Superficial liquid velocity, U_{sl}, seems to clearly affect the average value of *BSD*s only for the case of *Blood.* Apparently, as U_{sl} increases bubbles are sheared-off earlier from the surface of the glass filter. In *Water,* bubbles have reached their critical size (dictated mostly by capillarity) before their detachment even for the highest U_{sl} value and so $D_{1,0}$ does not vary considerably with U_{sl} (Fig. 8a and b). In *Blood*, however, the increased viscosity of the liquid decelerates bubble growth (i.e., convective radial expansion of the interface) at the surface of the glass filter. Therefore, as U_{sl} increases bubbles are sheared-off at early phases of their growth and therefore $D_{1,0}$ decreases as displayed in Fig. 9a and b. On the other hand, *CV* increases with U_{sl} only in *Water* for C_{SDS} = 5 ppm (Fig. 8c). For C_{SDS} = 500 ppm in *Water* and also for C_{SDS} = 0 ppm and C_{SDS} = 500 ppm in *Blood*, no persistent trend in *CV* is noticed. In *Water*, the rise of U_{sl} for C_{SDS} = 5 ppm intensifies turbulence and, consequently, increases the collision frequency of bubbles that enhances bubbles coalescence. Specifically in *Water,* Re_l = 860 for U_{sl} = 2.89 cm/s (laminar flow), Re_l = 2870 for U_{sl} = 9.62 cm/s (transition from laminar to turbulent flow) and Re_l = 4880, 6900, 8900 for U_{sl} = 16.36, 23.10, 29.83 cm/s respectively (turbulent flow). This might explain the formation of very large bubbles between 800 μm and 1200 μm (Fig. 4b) that augments the *CV* (Fig. 8c). In all other cases, bubbles coalescence is prevented by the high surfactant concentration or/and the increased liquid viscosity that suppresses turbulence (Re_l ranges from 140 to 1500 in *Blood*) so such large bubbles are not created (Figs. 5–7). It must be noted that the presence of bubbles increases the effect of turbulence above that indicated by the liquid phase Reynolds number (Re_l).

Surfactant concentration effect on *BSD* features is studied separately for the two test liquids. Fig. 8 shows that in *Water* the increase of C_{SDS} from 5 ppm to 500 ppm decreases substantially the average value and has a small – also decreasing- effect on the *CV*. This behavior may be attributed to the lower surface tension for C_{SDS} = 500 ppm which leads to smaller bubbles and to the appreciable surface elasticity that hinders bubbles coalescence, as also reported by other researchers, e.g. Elmahdy and Finch (2013) and Samaras et al. (2014). Similarly, in Blood the increase of C_{SDS} to 500 ppm shifts *BSD*s to smaller bubble sizes. However, this effect is less prominent than in *Water* since the high concentration of *NaCl* in *Blood* hinders bubbles coalescence already in the absence of surfactant (Xu et al., 2009). Contrary to *Water*, increasing the surfactant concentration in *Blood* makes *BSD*s broader (*CV* increases from ~70% to ~180%), Fig. 9c and d. At a first glance this seems peculiar as one might have expected a similar behavior with *Water*. The answer is hidden in the particular features of bubbly flow at these conditions as revealed by careful inspection of the obtained photos.

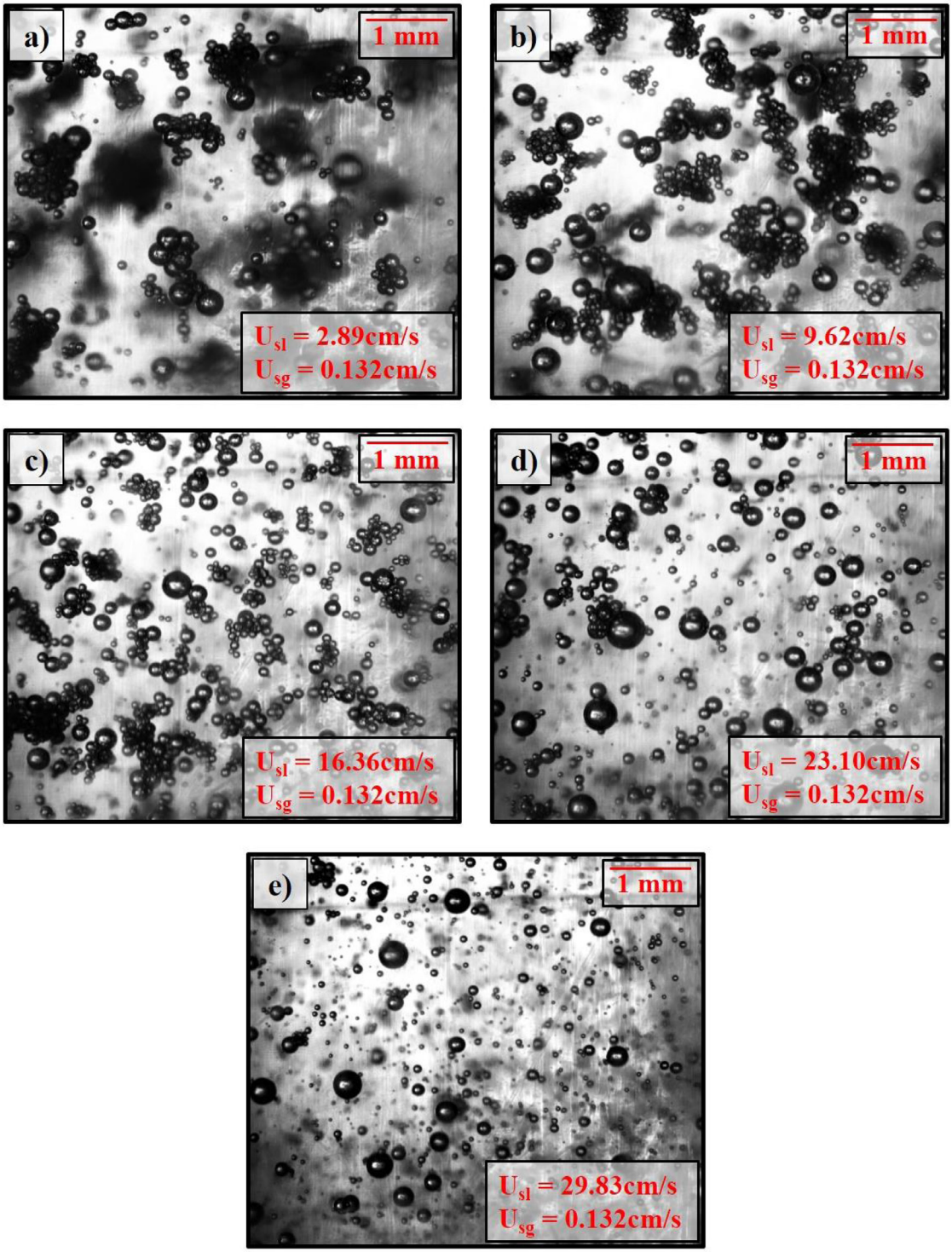

Fig. 10. Effect of superficial liquid velocity (U_{sl}) on the stability and size of bubble clusters in *Blood* for C_{SDS} = 500 ppm and U_{sg} = 0.132 cm/s: a) U_{sl} = 2.89 cm/s, b) U_{sl} = 9.62 cm/s, c) U_{sl} = 16.36 cm/s, d) U_{sl} = 23.10 cm/s, e) U_{sl} = 29.83 cm/s.

It is a distinct characteristic of the observed bubbly flow in *Blood,* Fig. 10, that bubbles form clusters rising among numerous (smaller) isolated bubbles. Bubble clusters result from the synergistic action of glycerol that increases liquid viscosity (Table 1), *NaCl* and *SDS*. The formation of bubble clusters is explained as follows: The molecules of *SDS* anionic surfactant are adsorbed at the surface of bubbles. In the absence of *NaCl* electrolyte, the adsorption coverage is limited due to the repulsive interactions between the adsorbed ionic surfactant molecules within the adsorption layer. The addition of *NaCl* electrolyte neutralizes the surface charge of adsorbed ionic surfactant molecules due to counter-ions adsorption. Consequently, the adsorption coverage of *SDS* over the surface of rising bubbles increases and results in higher surface viscosity and therefore lower bubble velocity (Krzan and Malysa, 2012; Jarek et al., 2010). In conclusion, bubbles can get close to each other as a result of electrostatic interactions damping, but they still cannot coalesce due to the *SDS* viscoelastic film that covers the bubbles (Jarvis et al., 2005; Xiao et al., 2011). At the same time, lower bubble velocity and increased liquid viscosity, due to glycerol addition,

causes longer contact time during bubbles collisions (Orvalho et al., 2015; Krzan and Malysa, 2012). Under these conditions, bubbles can form clusters of irregular shape, which are floppy and delicate and whose stability and size depends strongly on liquid superficial velocity. For low U_{sl} values (2.89 and 9.62 cm/s), bubble clusters maintain their integrity and their equivalent diameter can reach even 800 μm. As U_{sl} increases, however, bubble clusters become progressively smaller and their population is reduced dramatically (Fig. 10) as flow inertia is strong enough to decompose large clusters. This behavior has been also reported by Li et al. (2006) and Wang et al. (2011). It must be noted that Velez-Cordero and Zenit (2011) have noticed clusters in water/glycerol/xanthan mixtures in the presence of 0.04 M $MgSO_4$ that hampers coalescence. It seems that the key to cluster formation is to delay coalescence and this can occur even in the absence of adsorbed surfactant layers inasmuch as bulk viscosity is high enough to suppress shear stresses. More work is required in this direction to clarify the issue.

3.2. Experimental study of void fraction along the vertical pipe

Figs. 11–14 present average void fraction values calculated from 60 s long time series of *ERT* and *ΔP* measurements. Fig. 11 is meant to compare *ERT* and *ΔP* measurements. Fig. 11a and b present indicative local values of average void fraction versus superficial liquid velocity at a specific superficial gas velocity obtained at $z/D = 10$ and $z/D = 55$ from the gas injection point (porous filter), respectively. Fig. 11a refers to *Blood* with $C_{SDS} = 500$ ppm, while Fig. 11b concerns *Water* with $C_{SDS} = 500$ ppm. On the other hand, Fig. 11c displays indicative measurements of overall average void fraction in the vertical tube obtained from the $\Delta P_{overall}$ sensor and $ERT_{average}$, for $C_{SDS} = 500$ ppm in *Water*. Error bars indicating standard deviation values from repeated runs have been added to both *ERT* and *ΔP* data; in some cases error bars are smaller than data markers. Although *ERT* yields almost always a bit higher local void fraction values than *ΔP* (Fig. 11a and b), there is a fair agreement between the two measuring techniques. This is more so for the overall void fraction values if one takes into account the error bars (Fig. 11c). Jia et al. (2015) have also remarked a similar agreement between *ERT* and *ΔP* measurements in void fraction values lower than 0.2 in vertical upward bubbly flow.

Fig. 12a presents indicative *ERT* average void fraction values taken at three axial locations in the vertical tube, for $C_{SDS} = 500$ ppm in *Water*. Measurements are conducted for normalized axial distances of $z/D = 10$, $z/D = 30$ and $z/D = 55$ from the gas injection point. It is seen that in the examined distance range there is no significant axial variation of the measured void fraction. This observation is verified by differential pressure measurements, as shown in Fig. 12b for $C_{SDS} = 500$ ppm in *Blood*. In the latter figure, local void fraction measurements at $z/D = 10$ and $z/D = 55$ compare favorably with overall void fraction measurements in the vertical pipe. The axial uniformity of void fraction along the vertical pipe holds for both test liquids and for all experimental conditions. It is attributed chiefly to the absence of bubble breakup and coalescence along the examined distances. It is reasonable not to observe bubble breakup at such low superficial liquid velocities, i.e., weak turbulence (Hazuku et al., 2012), while bubble coalescence is hindered because of the *SDS* viscoelastic surface film and the low void fraction conditions (Tian et al., 2015). Thus, the examined upward bubbly flow can be considered as approximately uniform in the vertical tube at a distance of $z/D = 10$ as indicated by the axial uniformity of ERT and pressure drop measurements. Henceforth, all presented data correspond to measurements conducted with the $\Delta P_{overall}$ sensor. This is done for convenience but also because pressure measurements are more common and so they may allow direct comparison with other works in the future.

The influence of liquid superficial velocity (U_{sl}), gas superficial velocity (U_{sg}) and surface active agent concentration (C_{SDS}) on the measured void fraction is displayed in Figs. 13 and 14. Fig. 13 presents void fraction measurements for all examined U_{sl}, U_{sg} and C_{SDS} values in *Water,* while Fig. 14 presents the corresponding results for *Blood.* In both liquids, void fraction decreases when U_{sl} increases for a constant value of U_{sg} and C_{SDS}. As U_{sl} increases, bubbles flow at higher velocity and consequently their residence time inside the measuring volume

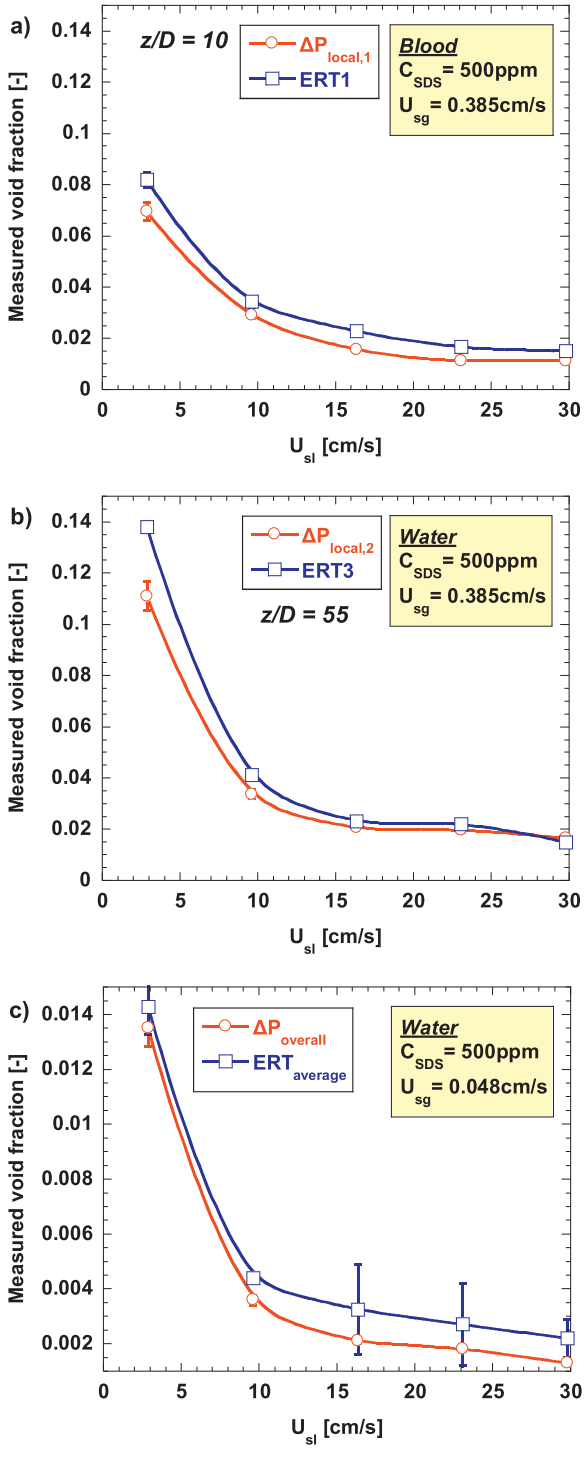

Fig. 11. Comparison of void fraction measurements between a) *ERT1* probe and $\Delta P_{local,1}$ sensor at a distance $z/D = 10$ from the gas injection point for *Blood* ($U_{sg} = 0.385$ cm/s, $C_{SDS} = 500$ ppm), b) *ERT3* probe and $\Delta P_{local,2}$ sensor at a distance $z/D = 55$ from the gas injection point for *Water* ($U_{sg} = 0.385$ cm/s, $C_{SDS} = 500$ ppm) and c) $ERT_{average}$ and $\Delta P_{overall}$ sensor for *Water* ($U_{sg} = 0.048$ cm/s, $C_{SDS} = 500$ ppm).

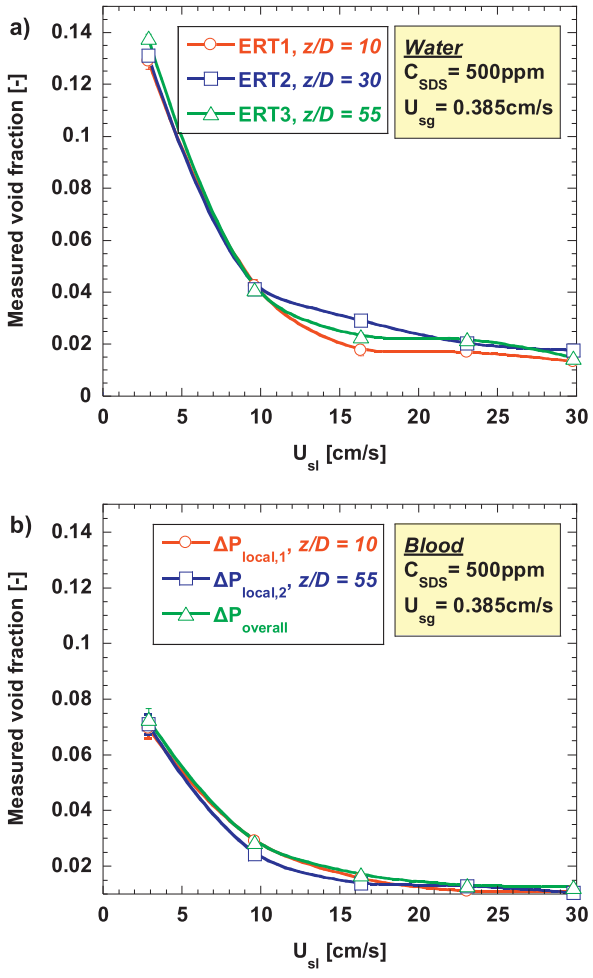

Fig. 12. Comparison of void fraction measurements along the vertical tube among a) *ERT1* ($z/D = 10$), *ERT2* ($z/D = 30$) and *ERT3* ($z/D = 55$) probes for *Water* (U_{sg} = 0.385 cm/s, C_{SDS} = 500 ppm), b) $\Delta P_{local,1}$ ($z/D = 10$), $\Delta P_{local,2}$ ($z/D = 55$) and $\Delta P_{overall}$ sensors for *Blood* (U_{sg} = 0.385 cm/s, C_{SDS} = 500 ppm).

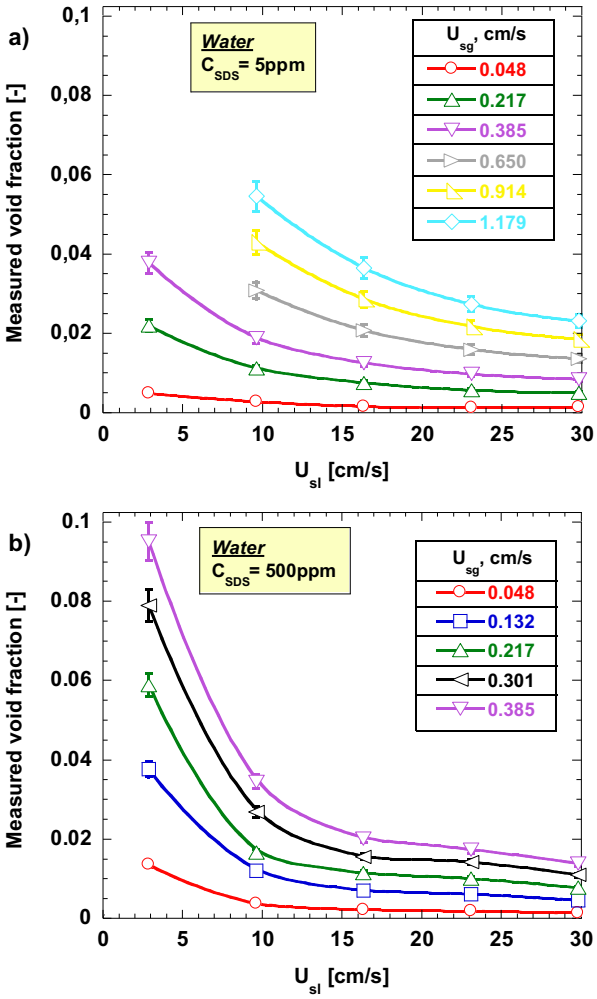

Fig. 13. Effect of superficial liquid velocity (U_{sl}) and superficial gas velocity (U_{sg}) on measured void fraction for: a) C_{SDS} = 5 ppm and b) C_{SDS} = 500 ppm, in *Water*.

drops yielding lower void fractions. It is noted that the variation of void fraction with U_{sl} is not linear with larger deviations observed at low U_{sl} values. Godbole et al. (2011) and Zhao et al. (2013) have also noticed the same trend. On the contrary, void fraction increases with rising U_{sg} for constant U_{sl} and C_{SDS} values, as more bubbles appear in the flow.

Void fraction increases with increasing C_{SDS}. Addition of *SDS* lowers the liquid surface tension and also increases the elasticity of bubble films hindering bubble coalescence (Xu et al., 2009). Therefore, more bubbles of smaller diameter rise inside the vertical tube. In *Water,* rise of C_{SDS} from 5 ppm to 500 ppm reduces the average bubble diameter ($D_{1,0}$) from 200–800 μm to 50–100 μm (Fig. 8a and b). In *Blood,* $D_{1,0}$ decreases from 150–350 μm to 50–200 μm with the addition of 500 ppm *SDS* despite the formation of bubble clusters (Fig. 9a and b). This is so because the number of these clusters is not large enough to induce $D_{1,0}$ increase and thereafter decrease of void fraction. For C_{SDS} = 500 ppm the surface of bubbles becomes immobile due to the presence of an adsorbed surfactant layer and consequently, drag coefficient increases towards that of a rigid sphere retarding surface motion. Thus, bubbles rise with lower velocity and their residence time in the tube increases resulting in higher void fraction (Alves et al., 2005). Although the effect of U_{sl}, U_{sg} and C_{SDS} on the measured void fraction is qualitatively similar for the two liquids, it differs from a quantitative point of view. This can be attributed to the different features of bubble size distributions due to the varying physicochemical properties of the two liquids.

4. Conclusions

This work investigates experimentally Bubble Size Distributions (*BSD*) and void fractions in a gas–liquid flow of small bubbles (< 1 mm) at low void fractions ($<10^{-1}$) that resembles bubbly flow in human vena cava during Decompression Sickness. Similar bubbly flow conditions can be also found in other two-phase systems such as flow boiling in macro-channels. Determination of *BSDs* is based on an optical method that captures high resolution bubbly flow images and their analysis by advanced image processing algorithms to deal with overlapping bubbles. Cross-sectional area averaged and volumetric void fraction is measured along the pipe by means of Electrical Resistance Tomography (*ERT*) and Differential Pressure method (ΔP), respectively. Experiments are conducted in water and blood simulant, while bubble size varies using prescribed surfactant (*SDS*) concentrations. It is seen that bubbly flow is approximately uniform along the vertical pipe as indicated from *ERT* measurements at three axial locations combined with local and global ΔP measurements. It is demonstrated that *BSDs* are well-fitted with log-normal distributions. *BSDs*' average values increase with superficial gas velocity due to higher gas flow rate but also enhancement of bubbles coalescence. On the contrary, increase of surfactant concentration prevents bubbles coalescence leading to reduction of bubbles average diameter. Interestingly, the addition of 500 ppm *SDS* in blood simulant results in the formation of bubble clusters due to the synergistic action of glycerol that increases liquid

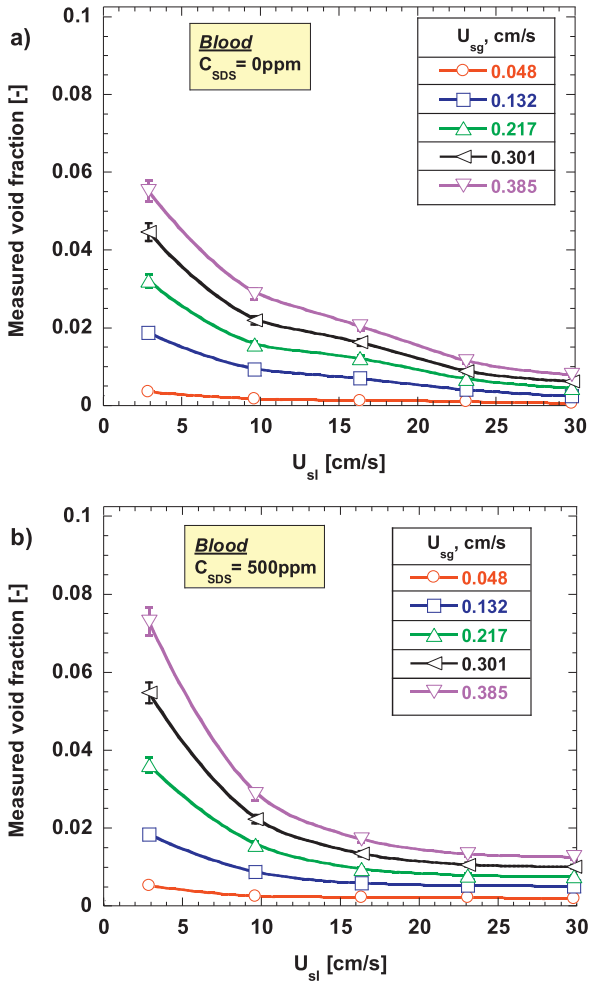

Fig. 14. Effect of superficial liquid velocity (U_{sl}) and superficial gas velocity (U_{sg}) on measured void fraction for: a) C_{SDS} = 0 ppm and b) C_{SDS} = 500 ppm, in *Blood*.

viscosity, *NaCl* electrolyte and *SDS* surfactant. These clusters make *BSDs* broader. Yet, as liquid superficial velocity increases the size and population of clusters is reduced due to the action of flow inertia. Concerning void fraction, *ERT* and *ΔP* measurements are in fair agreement to each other for all experimental conditions. Moreover, void fraction increases with increasing gas superficial velocity, increasing surfactant concentration and decreasing liquid superficial velocity.

Acknowledgments

This study was funded by esa (GSTP Project: In-Vivo Embolic Detector, I-VED – Contract No.: 4000101764 and MAP Project: Convective boiling and condensation local analysis and modelling of dynamics and transfers, MANBO – Contract No.: 4200020289) and carried out under the umbrella of COST Action MP1106: 'Smart and green interfaces—from single bubbles and drops to industrial, environmental and biomedical applications' and COST Action MP1305: 'Flowing Matter'. The view expressed herein can in no way be taken to reflect the official opinion of the European Space Agency.

Supplementary materials

Supplementary material associated with this article can be found, in the online version, at doi:10.1016/j.ijheatfluidflow.2018.04.011.

References

Alves, S.S., Orvalho, S.P., Vasconcelos, J.M.T., 2005. Effect of bubble contamination on rise velocity and mass transfer. Chem. Eng. Sci. 60, 1–9.
Antle, C.E., 1985. Encyclopedia of Statistical Sciences. John Wiley and Sons, New York.
Besagni, G., Inzoli, F., 2016. Bubble size distributions and shapes in annular gap bubble column. Exp. Therm. Fluid Sci. 74, 27–48.
Bhagwat, S.M., Ghajar, A.J., 2014. A flow pattern independent drift flux model based void fraction correlation for a wide range of gas–liquid two phase flow. Int. J. Multiphas. Flow 59, 186–205.
Chatzidafni, A., Evgenidis, S., Lioumbas, J., Karapantsios, T., 2009. Electrical resistance tomography in upward co-current bubbly flow. In: 4th International Workshop "Bubble and Drop Interfaces", Thessaloniki, Greece.
Deckwer, W.D., 1992. Bubble Column Reactors. John Wiley and Sons, England.
Dorsey, N.E., 1940. Properties of Ordinary Water-Substances. New York.
Dutschk, V., Karapantsios, T., Liggieri, L., McMillan, N., Miller, R., Starov, V.M., 2014. Smart and green interfaces: from single bubbles/drops to industrial environmental and biomedical applications. Adv. Colloid. Interface Sci. 209, 109–126.
Elmahdy, A.M., Finch, J.A., 2013. Effect of frother blends on hydrodynamic properties. Int. J. Miner. Process 123, 60–63.
Evgenidis, S., Karapantsios, T., 2015. Effect of bubble size on void fraction fluctuations in dispersed bubble flows. Int. J. Multiph. Flow 75, 163–173.
Evgenidis, S., Kazakis, N.A., Karapantsios, T.D., 2010. Bubbly flow characteristics during decompression sickness: effect of surfactant and electrolyte on bubble size distribution. Colloids Surf. A: Physicochem. Eng. Aspects 365, 46–51.
Fransolet, E., Crine, M., Marchot, P., Toye, D., 2005. Analysis of gas holdup in bubble columns with non-Newtonian fluid using electrical resistance tomography and dynamic gas disengagement technique. Chem. Eng. Sci. 60, 6118–6123.
Gaillard, T., Honorez, C., Jumeau, M., Elias, F., Drenckhan, W., 2015. A simple technique for the automation of bubble size measurements. Colloids Surf. A: Physicochem. Eng. Aspects 473, 68–74.
Godbole, P.V., Tang, C.G., Ghajar, A.J., 2011. Comparison of void fraction correlations for different flow patterns in upward vertical two-phase flow. Heat Transfer Eng 32 (10), 843–860.
Grau, R., Heiskanen, K., 2005. Bubble size distribution in laboratory scale flotation cells. Miner. Eng. 180 (12), 1164–1172.
Han, Y.F., Zhao, A., Zhang, H.X., Ren, Y.Y., Liu, W.X., Jin, N.D., 2016. Differential pressure method for measuring water holdup of oil–water, two-phase flow with low velocity and high water-cut. Exp. Therm. Fluid Sci. 72, 197–209.
Hazuku, T., Takamasa, T., Hibiki, T., 2012. Characteristics of developing vertical bubbly flow under normal and microgravity conditions. Int. J. Multiph. Flow 38, 53–66.
Hills, J.H., 1976. The operation of a bubble column at high throughputs. Chem. Eng. J. 12, 89–99.
Jarvis, P., Jefferson, B., Gregory, J., Parsons, S.A., 2005. A review of floc strength and breakage. Water Res 39, 3121–3137.
Jarek, E., Jasinski, T., Barzyk, W., Warszynski, P., 2010. The pH regulated surface activity of alkanoic acids. Colloids Surf. A. 354, 188–196.
Jia, J., Babatunde, A., Wang, M., 2015. Void fraction measurement of gas–liquid two-phase flow from differential pressure. Flow Meas. Instrum. 41, 75–80.
Jin, H., Lian, Y., Yang, S., He, G., Guo, Z., 2013. The parameters measurement of air–water two phase flow using the electrical resistance tomography (ERT) technique in a bubble column. Flow Meas. Instrum. 31, 55–60.
Jin, H., Wang, M., Williams, R.A., 2006. The effect of sparger geometry on gas bubble flow behaviors using electrical resistance tomography. Chinese J. Chem. Eng. 14, 127–131.
Jin, H., Yang, S., He, G., Wang, M., Williams, R.A., 2010. The effect of gas–liquid counter-current operation on gas hold-up in bubble columns using electrical resistance tomography. J. Chem. Technol. Biotechnol. 85, 1278–1283.
Julia, J.E., Hibiki, I., 2011. Flow regime transition criteria for two-phase flow in a vertical annulus. Int. J. Heat Fluid Fl. 32, 993–1004.
Kanizawa, F.T., Ribatski, G., 2017. Void fraction and pressure drop during external upward two-phase crossflow in tube bundles – part I: experimental investigation. Int. J. Heat Fluid Fl. 65, 200–209.
Karn, A., Ellis, C., Arndt, R., Hong, J., 2015. An integrative image measurement technique for dense bubbly flows with a wide size distribution. Chem. Eng. Sci. 122, 240–249.
Krzan, M., Malysa, K., 2012. Influence of electrolyte presence on bubble motion in solutions of sodium-alkylsulfates (C8-C10-C12). Physicochem. Probl. Miner. Process. 48 (1), 49–62.
Lau, Y.M., K. Thiruvalluvan Sujatha, K., Gaeini, M., Deen, N.G., Kuipers, J.A.M., 2013. Experimental study of the bubble size distribution in a pseudo-2D bubble column. Chem. Eng. Sci. 98, 203–211.
Li, T., Zhu, Z., Wang, D., Yao, C., Tang, H., 2006. Characterization of floc size, strength and structure under various coagulation mechanisms. Powder Technol 168, 104–110.
Lioumbas, J., Chatzidafni, A., Karapantsios, T., 2014. Spatial considerations on electrical resistance tomography measurements. Meas. Sci. Technol. 25, 1–12.
Majumder, S., Kundu, G., Mukherjee, D., 2006. Bubble size distribution and gas–liquid interfacial area in a modified downflow bubble column. Chem. Eng. J. 122, 1–10.
Maurus, R., Ilchenko, V., Sattelmayer, T., 2002. Study of the bubble characteristics and the local void fraction in subcooled flow boiling using digital imaging and analyzing techniques. Exp. Therm. Fluid. Sci. 26, 147–155.
Maxwell, J.C., 1892. A Treatise of Electricity and Magnetism. Oxford University Press, London.
Meng, Z., Huang, Z., Wang, B., Ji, H., Li, H., Yan, Y., 2010. Air–water two-phase flow measurement using a venture meter and an electrical resistance tomography sensor. Flow Meas. Instrum. 21, 268–276.

Merchuk, J.C., Stein, Y., 1981. Local hold-up and liquid velocity in air-lift reactors. A.I.Ch.E. J. 27, 377–388.
Merkus, H.G., 2009. Particle Size Measurements: Fundamentals, Practice, Quality. Springer.
Mino, K., Imura, M., Koyama, D., Omori, M., Kawarabata, S., Sata, M., Watanabe, Y., 2015. Meshless bubble filter using ultrasound for extracorporeal circulation and its effect on blood. Ultrasound in Med. & Biol. 41 (2), 465–471.
Oikonomidou, O., Evgenidis, S.P., Kostoglou, M., Karapantsios, T.D., 2018. Degassing of a pressurized liquid saturated with dissolved gas when injected to a low pressure liquid pool. Exp. Therm. Fluid Sci. 96, 347–357.
Orvalho, S., Ruzicka, M.C., Olivieri, G., Marzocchella, A., 2015. Bubble coalescence: effect of bubble approach velocity and liquid viscosity. Chem. Eng. Sci. 134, 205–216.
Papadopoulou, V., Evgenidis, S., Eckersley, R.J., Mesimeris, T., Balestra, C., Kostoglou, M., Karapantsios, T.D., Tang, M.X., 2015. Decompression induced bubble dynamics on ex vivo fat and muscle tissue surfaces with a new experimental set up. Colloids Surf. B: Biointerfaces 129, 121–129.
Riquelme, A., Desbiens, A., del Villar, R., Maldonado, M., 2015. Identification of a non-linear dynamic model of the bubble size distribution in a pilot flotation column. Int. J. Miner. Process. 145, 7–16.
Samaras, K., Kostoglou, M., Karapantsios, T., Mavros, P., 2014. Effect of adding glycerol and Tween 80 on gas holdup and bubble size distribution in an aerated stirred tank. Colloids Surf. A: Physicochem. Eng. Aspects 441, 815–824.
Shen, X., Sun, H., Deng, B., Hibiki, T., Nakamura, H., 2017. Experimental study on interfacial area transport of two-phase bubbly flow in a vertical large-diameter square duct. Int. J. Heat Fluid Fl. 67, 168–184.
Tang, C., Heindel, T.J., 2006. Estimating gas holdup via pressure difference measurements in a cocurrent bubble column. Int. J. Multiph. Flow 32, 850–863.
Tang, C., Heindel, T.J., 2007. Effect of fiber length distribution on gas holdup in a concurrent air-water-fiber bubble column. Chem. Eng. Sci. 62, 1408–1417.
Tian, D., Yan, C., Sun, L., 2015. Evaluation of interfacial area transport equation in vertical bubbly two-phase flow in large diameter pipes. Ann. Nucl. Energy 75, 199–209.
Uesawa, S.I., Kaneko, A., Abe, Y., 2012. Measurement of void fraction in dispersed bubbly flow containing micro-bubbles with the constant electric current method. Flow Meas. Instrum. 24, 50–62.
Vann, R.D., Butler, F.K., Mitchell, S.J., Moon, R.E., 2011. Decompression illness. The Lancet 377, 153–164.
Velez-Cordero, J.R., Zenit, R., 2011. Bubble cluster formation in shear-thinning inelastic bubbly columns. J. Non-Newtonian Fluid Mech. 166, 32–41.
Wang, D., Wu, R., Jiang, Y., Chow, C.W.K., 2011. Characterization of floc structure and strength: role of changing shear rates under various coagulation mechanisms. Colloids Surf. A: Physicochem. Eng. Aspects 379, 36–42.
Woodcock, J.P., 1975. Physical properties of blood and their influence on blood-flow measurement. Rep. Prog. Phys. 39, 65–127.
Xiao, F., Lam, K.M., Li, X.Y., Zhong, R.S., Zhang, X.H., 2011. PIV characterization of flocculation dynamics and floc structure in water treatment. Colloids Surf. A: Physicochem. Eng. Aspects 379, 27–35.
Xu, Q., Nakajima, M., Ichikawa, S., Nakamura, N., Roy, P., Okadome, H., Shiina, T., 2009. Effects of surfactant and electrolyte concentrations on bubble formation and stabilization. J. Colloid Interface Sci. 332, 208–214.
Yoo, J., Estrada-Perez, C.E., Hassan, Y.A., 2016. Experimental study on bubble dynamics and wall heat transfer arising from a single nucleation site at subcooled flow boiling conditions – part 1: experimental methods and data quality verification. Int. J. Multiph. Flow 84, 315–324.
Zabulis, X., Papara, M., Chatziargyriou, A., Karapantsios, T.D., 2007. Detection of densely dispersed spherical bubbles in digital images based on a template matching technique: application to wet foams. Colloids Surf. A: Physicochem. Eng. Aspects 309, 96–106.
Zhao, Y., Bi, Q., Hu, R., 2013. Recognition and measurement in the flow pattern and void fraction of gas–liquid two-phase flow in vertical upward pipes using the gamma densitometer. Appl. Therm. Eng. 60, 398–410.